



Low Frequency Quasi-periodic Oscillations in the High-eccentric LMXB Cir X-1: Extending the WK Correlation for Z Sources

Qingcui Bu^{1,2}, T. M. Belloni², Li Chen¹, and Jinlu Qu³

¹ Department of Astronomy, Beijing Normal University, Beijing 100875, China; buqc@mail.bnu.edu.cn

² INAF-Osservatorio Astronomico di Brera, Via E. Bianchi 46, I-23807 Merate (LC), Italy; tomaso.belloni@brera.inaf.it

³ Laboratory for Particle Astrophysics, CAS, Beijing 100049, China; chenli@bnu.edu.cn, qujl@ihep.ac.cn

Received 2016 December 19; revised 2017 April 26; accepted 2017 April 27; published 2017 June 2

Abstract

Using archival *Rossi X-ray Timing Explorer (RXTE)* data, we studied the low-frequency quasi-periodic oscillations (LFQPOs) in the neutron star low-mass X-ray binary (LMXB) Cir X-1 and examined their contribution to frequency–frequency correlations for Z sources. We also studied the orbital phase effects on the LFQPO properties and found them to be phase independent. Comparing LFQPO frequencies in different classes of LMXBs, we found that systems that show both Z and atoll states form a common track with atoll/BH sources in the so-called WK correlation, while persistent Z systems are offset by a factor of about two. We found that neither source luminosity nor mass accretion rate is related to the shift of persistent Z systems. We discuss the possibility of a misidentification of fundamental frequency for horizontal branch oscillations from persistent Z systems and interpreted the oscillations in terms of models based on relativistic precession.

Key words: accretion, accretion disks – black hole physics – stars: general – stars: neutron – X-rays: binaries – X-rays: stars

1. Introduction

Low-frequency quasi-periodic oscillations (LFQPOs) are widely detected in low-mass X-ray binaries (LMXBs). They appear as narrow peaks in power spectra with frequencies varying from a few millihertz to tens of hertz (Homan et al. 2002; van der Klis 2006; Belloni et al. 2007), along with several broadband components (Casella et al. 2005; Motta 2016).

Atoll sources and Z sources are subclasses of neutron star (NS)-LMXBs based on their X-ray timing and spectral properties (Hasinger & van der Klis 1989). Z sources typically trace a “Z” pattern in their color–color diagrams (CDs) and hardness–intensity diagrams (HIDs) with three branches: the horizontal branch (HB), the normal branch, and the flaring branch. Consequently, LFQPOs in Z sources are then classified into three subgroups: horizontal branch oscillations (HBOs), normal branch oscillations, and flaring branch oscillations. Black hole (BH)-LMXBs also have three types of LFQPOs called types A, B, and C (Wijnands et al. 1999; Cui et al. 2000; Remillard et al. 2002; Casella et al. 2004; Motta et al. 2011; Zhang 2013). Type-C QPOs are the most common type: a comparison of their power spectra with HBOs in NS-LMXBs suggests that they may have a similar origin (Psaltis et al. 1999; Wijnands & van der Klis 1999; Belloni et al. 2002; Casella et al. 2005).

There is still no universal explanation for LFQPOs in X-ray binaries, although several models have been proposed to explain their origin (Stella & Vietri 1998; Tagger & Pellat 1999; Titarchuk & Osherovich 1999; Ingram et al. 2009; Motta et al. 2015a). A large amount of work has been done on BH-LFQPOs and showed evidence for a relativistic Lense–Thirring (LT) precession origin for type-C QPOs (Schnittman et al. 2006; Ingram et al. 2009; Motta et al. 2015b). Compared to BH-LFQPOs, studies in NS-LFQPOs are dispersed, mostly focused on single sources, leading to the suggestion that NS-LFQPOs also have a geometric origin (Altamirano et al. 2012;

Homan 2012; Homan et al. 2015). However, LT precession becomes controversial when it comes to NS-LMXBs sources, especially for Z sources (Altamirano et al. 2012; Li et al. 2013, 2014; Bu et al. 2015). LFQPOs in Z sources have not been studied in similar detail to make a full comparison with BH-LMXBs, due to their fast changes in spectra properties and the extra boundary layer outside the compact object. However, correlations between characteristic frequencies of QPOs and noise (the so-called WK and PBK correlations; Psaltis et al. 1999; Wijnands & van der Klis 1999) provide a valuable way to compare LFQPOs as they apply to Z sources, atoll sources, and BH-LMXBs.

In this paper, we study the LFQPOs and low-frequency noise observed in Cir X-1, which shows the most complex properties seen among known NS-LMXBs (with the exception of the very peculiar rapid burster). The temporal behavior along its HIDs suggested that Cir X-1 is a peculiar Z source (Oosterbroek et al. 1995; Shirey 1998; Qu et al. 2001). Fridriksson et al. (2015) also suggested that Cir X-1 has shown the broadest range in secular evolution: it displayed Cyg-like and Sco-like Z tracks in the CD/HID, as well as atoll soft and hard states, and entered a near-quiescence state. The binary has a ~ 16.6 days orbital period, which was first identified from periodic flaring in the X-ray band (Kaluzienski et al. 1976). When it is active, the spectral and temporal characteristics of Cir X-1 are correlated with its orbital phase (Shirey et al. 1996; Ding et al. 2006). The X-ray emission from Cir X-1 is highly variable on a wide range of timescales (Parkinson et al. 2003). All these features make it a very good source to study LFQPOs in NS-LMXBs. Based on our previous work on XTE J1701–462 and GX 17+2 (Bu et al. 2015), we extend our analysis to Cir X-1 as a peculiar Z source.

In this work, we used *Rossi X-ray Timing Explorer (RXTE)*/Proportional Counter Array (PCA) satellite data of Cir X-1 to compare its properties to those of other systems, as well as to study their dependence on orbital phase.

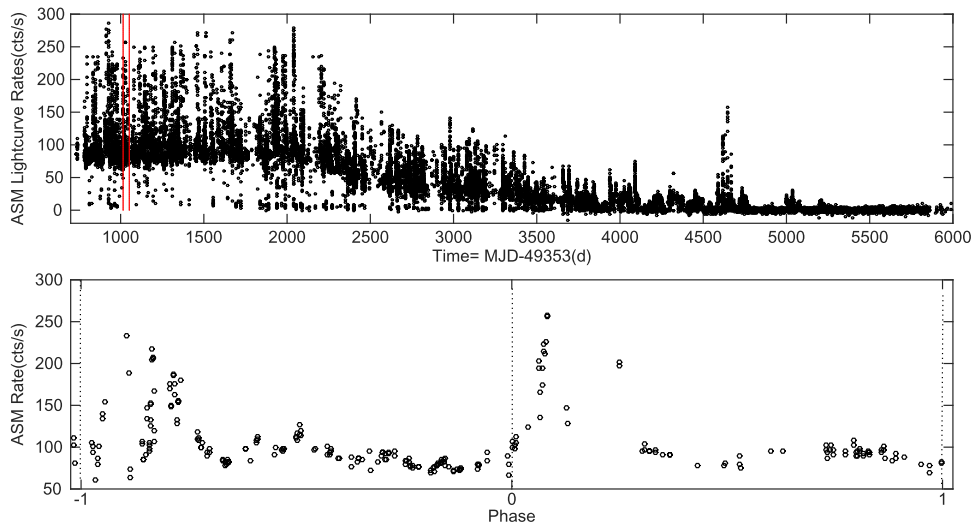


Figure 1. Upper panel: *RXTE* ASM light curve of Cir X-1 in the energy band 2–12 keV, covering the entire life of the *RXTE* mission. Lower panel: two complete orbital cycles observed with the ASM, extracted from the time period marked by red lines in the upper panel. The vertical dotted lines indicate phase zero. Data points are 90 s averages.

2. Data Reduction and Analysis

2.1. Data Selection

We analyzed all the public data of Cir X-1, 811 observations, collected with the *RXTE*/PCA. The X-ray light curve of Cir X-1 from the All-sky Monitor (ASM) on board *RXTE* is shown in Figure 1 (upper panel). It was one of the brightest NS-LMXB sources at ~ 3 Crab level (1 Crab ~ 75 ASM cts s^{-1}) from 1996 to 2000, but its luminosity steadily decreased from 2000 to 2006, reaching a near-quietest state in 2007.

2.2. Timing Analysis

We used the HEASOFT 6.16 package to analyze all the data, filtering data with elevation angle $> 10^\circ$, pointing offset < 0.01 , and South Atlantic Anomaly exclusion times of 30 minutes.

Cir X-1 is known to show type-I X-ray bursts. We removed all nine bursts reported in the literature (Linares et al. 2010). We used single-bit (SB) and event (E) mode data with time resolutions smaller than 2^{-11} s to create light curves. No background-subtraction or dead-time correction were applied. A power density spectrum (PDS) for each observation was computed from 32 s time stretches, with a Nyquist frequency of 1024 Hz. The PDS from each stretch were then averaged together to obtain one PDS per observation. We computed the PDS using all active proportional counter units (PCUs) in the energy band 2–60 keV. Standard fast Fourier transform (FFT) techniques were used to create PDS and applied to the rms normalization from Belloni & Hasinger (1990).

We fitted all the PDS with the XSPEC (version 12.9.0; Arnaud 1996) package using a unit response. We chose as a model a multi-Lorentzian function (plus a power law at low frequencies when necessary) to fit all the components (QPOs and noise) in the PDS (Nowak 2000; Belloni et al. 2002). The characteristic frequency ν_{\max} of the Lorentzian is given by $\nu_{\max} = \sqrt{\nu_0^2 + \Delta^2}$ (Belloni et al. 2002), where ν_0 is the Lorentzian’s centroid frequency and Δ its HWHM.

Since the data span ~ 15 years, the instrument gain is different for different observing periods. However, if we consider the whole energy band, the influence of energy

changes can be neglected. In this paper, we mainly studied the QPO properties and gain changes were not considered.

3. Results

3.1. Frequency–Frequency Correlation in Cir X-1 and Z Sources

We computed PDS for all 811 observations in Cir X-1, and in 149 of them, we detected significant LFQPO components (with the quality factor $Q = \nu_0/2\Delta$ higher than 2 and significance larger than 3σ). Figure 3 shows a long-term light curve of the source, with each data point being the average of one observation. The observations with detected LFQPOs are marked with colored points, as are the observations already reported by Shirey et al. (1996, 1998) and Fridriksson et al. (2015), who identified the LFQPOs as HBOs. LFQPOs occur over a large range of intensity, and their significance level (defined as the integral of the Lorentzian fitting the peak in PDS divided by its error) ranges between 3σ to 25σ .

The first observations of Cir X-1 in the atoll hard state took place on 2010 May/June (MJD = 55327), after almost 15 years of dense *RXTE* coverage. In order to study the source state after MJD 55327, in Figure 2, we plot a color–color diagram of the observations after MJD 55327; the observations of atoll hard state reported by Fridriksson et al. (2015) are plotted in red. The plot shows that all observations after that date (black dots) are consistent with those observations from confirmed atoll states (red dots), confirming that Cir X-1 exhibits an atoll state after MJD 55327. Of course, appearances of an atoll state might have taken place before that date, but the QPO detections by Shirey et al. (1996, 1998) and Fridriksson et al. (2015) have been confirmed as HBOs. Among the 149 LFQPOs observations, we have found 144 before MJD 55327 and 5 after MJD 55327 in the atoll state (red stars in Figure 3). Judging by the presence of a low-frequency flat-top noise in PDS, we classified 117 QPOs as possible HBOs. These QPOs have a centroid frequency between ~ 1 and ~ 50 Hz, while the 5 LFQPOs observed in the atoll state have centroid frequencies between ~ 5 and ~ 17 Hz. As mentioned above, some of these QPOs might be from an unrecognized atoll phase, so we plot them with different symbols than those

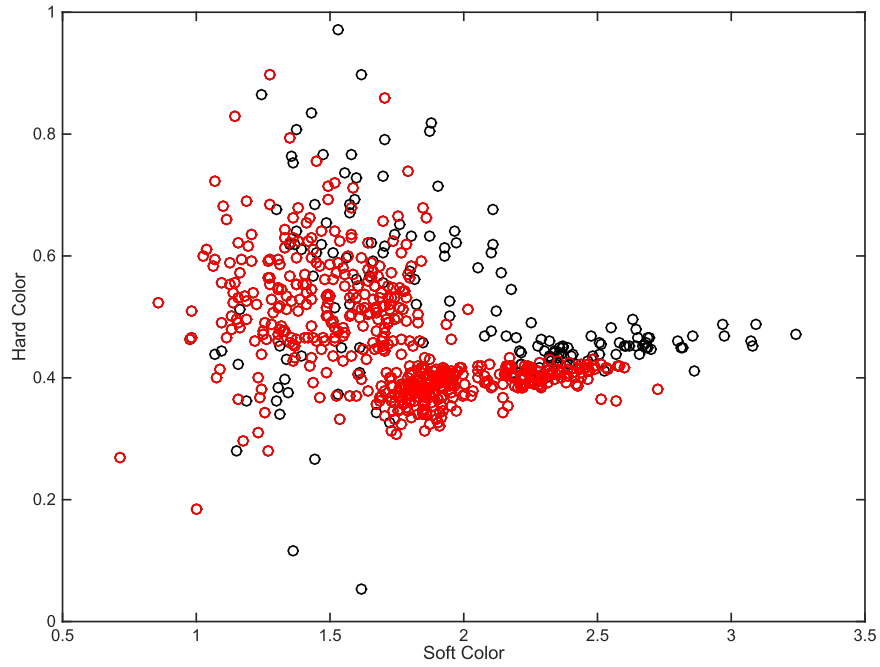


Figure 2. Color-color diagram for the observations from MJD 55327–55764. In the CD, soft color is defined as the ratio of count rate in the 5.3–6.9 keV/4.1–5.3 keV bands, and hard color is defined as the ratio in the 10.6–22.3 keV/6.1–10.6 keV bands. Observations from Fridriksson et al. (2015) are plotted as red points, which are confirmed as atoll state, corresponding to MJD 55343.4–55350.7.

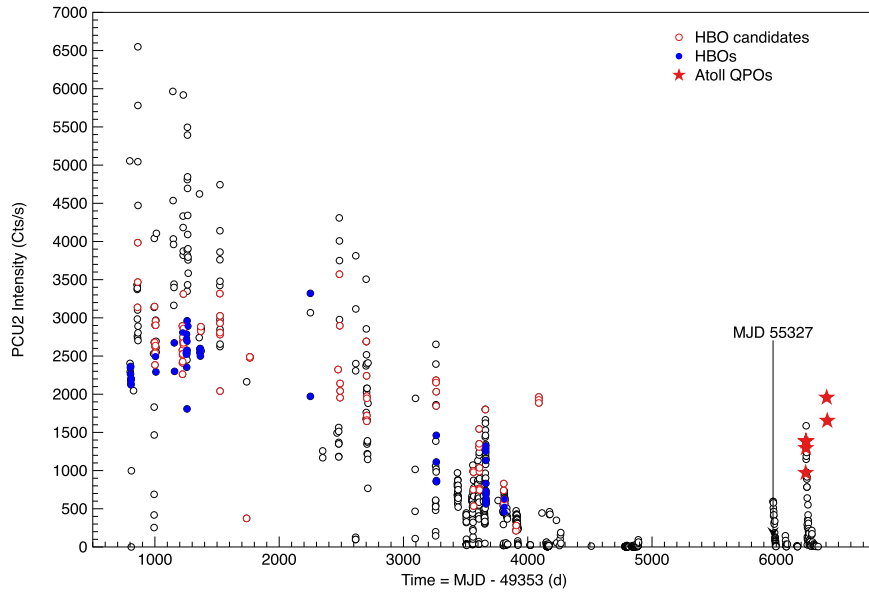


Figure 3. A long-term light curve of the source extracted from energy band 2–12 keV, with each data point being the average of one observation. Only PCU2 data is used. Observations with significant LFQPOs are indicated with red dots, and the QPOs confirmed as HBOs are marked with blue points (Shirey et al. 1996, 1998; Fridriksson et al. 2015). QPOs from atoll states are marked as red stars. The transition time MJD 55327 is indicated in the plot.

in Shirey et al. (1996, 1998) and Fridriksson et al. (2015), which were identified as HBOs. These are 49 QPOs within our sample of 117, marked as blue dots in Figure 3, with the remainder of the sample named as HBO candidates. In this section, we mainly study the timing features of 122 LFQPO observations, including 49 HBOs, 68 HBO candidates, and 5 QPOs from the atoll state.

The FWHM and fractional rms amplitude of 122 LFQPOs as a function of its centroid frequency are plotted in Figure 4. The FWHM of HBOs generally increases with their frequencies, with Q values between 2 and 10, while LFQPOs from the atoll state show a constant Q factor around 5. Fractional rms

generally decreases with QPO frequency from 12% to 2% both for HBOs and atoll points. There is no difference between HBOs and HBO candidates in these plots.

In Figure 5, we show six representative PDS from the sample. Each individual component of the multi-Lorentzian best fit is also shown. We only plotted frequencies up to 128 Hz since we focus on low-frequency components. All of the LFQPOs (L_{LF}) are accompanied by several broadband components: occasionally a very low frequency noise (L_{VLFN}), a low-frequency broad component (L_b), sometimes a sub-harmonic of the LFQPO (L_{subh}), a hump (L_h), or a second harmonic component (L_{har}), and a high-frequency noise component (L_{hn}).

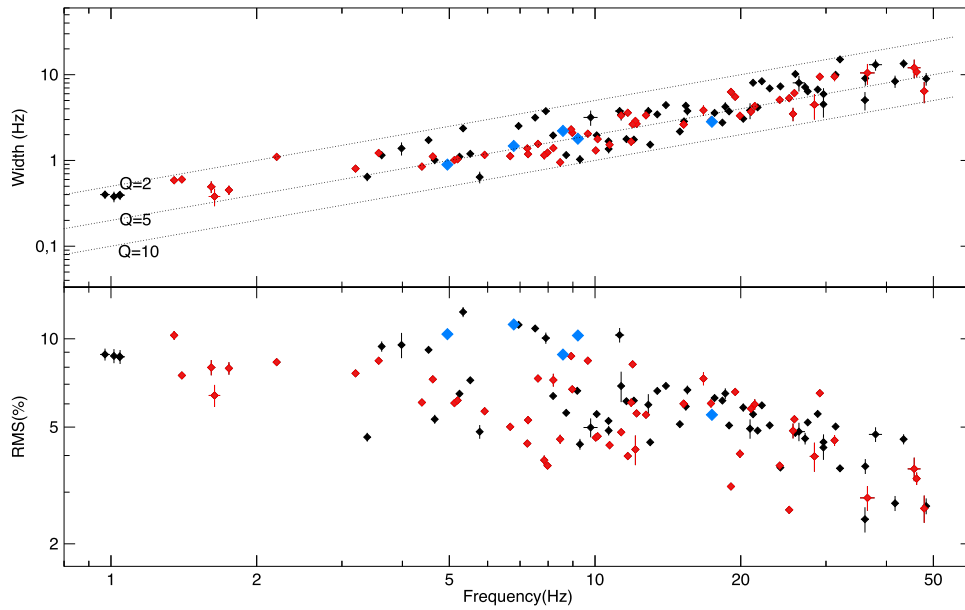


Figure 4. Upper panel: LFQPO width as a function of its centroid frequency. Each point represents a single observation. LFQPOs from the atoll state are marked with blue diamonds, confirmed HBOs are marked as red diamonds, and HBO candidates are plotted as black diamonds. The dotted lines indicate different Q values, from 2 to 10. Lower panel: LFQPO fractional rms as a function of its centroid frequency.

LFQPOs are easy to detect and identify because of their high quality factor, while L_b has to be identified among the remaining components in the PDS. Generally, we define L_b as the first noise component below the LFQPO, or below the sub-harmonic if this is detected. Whether to include a sub-harmonic or not in the fitted model was judged by the goodness of fit (reduced chi-square). In Figure 6, we show two pairs of PDSs with similar LFQPOs at ~ 5 and ~ 10 Hz, with and without significant sub-harmonics. Among the 122 observations, we found 50 of them with a significant sub-harmonic. In order to check whether the L_{bar} is really a sub-harmonic, in Figure 7, we plot its centroid frequency as a function of that of the LFQPO. The points follow a $y = 2x$ relation, confirming the harmonic relation. For those observations without significant sub-harmonics, in order to have a homogeneous model for all PDSs, we also included a sub-harmonic component with a central frequency at half of the LFQPO centroid frequency.

Figure 8 shows the characteristic frequency of the LFQPO as a function of the characteristic frequency ν_{break} of the L_b component, including HBOs, HBO candidates, and LFQPOs from the atoll state. This is the so-called WK correlation (Wijnands & van der Klis 1999). The result shows HBOs, HBO candidates, and LFQPOs from the atoll state are consistent with each other in the WK correlation. The figure also includes the original points from Wijnands & van der Klis (1999) and XTE J1701-462 points from Bu et al. (2015). The lines in the figure are the best-fit power laws to BH/atoll sources, Z sources, and Cir X-1. The best-fit models are: $\nu_{\text{LFQPO}} = (5.2 \pm 0.32) * \nu_{\text{break}}^{(0.81 \pm 0.03)}$ for BH/atoll sources, $\nu_{\text{LFQPO}} = (15.7 \pm 2.8) * \nu_{\text{break}}^{(0.62 \pm 0.22)}$ for Z sources, and $\nu_{\text{LFQPO}} = (5.4 \pm 0.44) * \nu_{\text{break}}^{(0.86 \pm 0.08)}$ for Cir X-1. Errors are quoted at 95% confidence. Since Wijnands & van der Klis (1999) did not include uncertainties in the original points, we assigned to them a 5% representative error. The Cir X-1 points follow a correlation that is formally consistent with that of BH/atoll and overlap at high frequencies with that of XTE

J1701-462. Yet, Z sources are clearly offset, as already pointed out by Wijnands & van der Klis (1999). In order to check its offset quantitatively, in Figure 9, we plot the histogram of the ratio between the LFQPO frequencies and the best-fitting line for atoll/BH sources. From Figure 9, we can see that Z sources cluster around a factor of two higher frequency, while XTE J1701-462 has a small offset.

The Cir X-1 frequencies were extracted from full observations. In order to check whether selecting PDS along the CD produces different results, we accumulated PDS from the regions in the Z tracks from Fridriksson et al. (2015). This led to HBO frequencies restricted to the 8–30 Hz range only, but the associated points in the WK correlation are consistent with those in Figure 7.

3.2. Orbital Effects on LFQPOs

We also studied the orbital phase dependence of time properties, since connections were found previously (Shirey 1998). We used a revised ephemeris $\text{JD}_0 = 2450082.54 + (16.54694 - 0.0000353N)N$ by Shirey (1998) to calculate the orbital phase (ϕ) for each observation. Here, JD_0 is the time of zero phase and N is the number of cycles counting immediately after the launch of *RXTE* (1995 December 30). The quadratic term of the equation indicates that the period is decreasing by ~ 2 minutes yr^{-1} ($\dot{P} = 4.3 * 10^{-6} = 134 \text{ s yr}^{-1}$). Phase errors are calculated by the error propagations from the equation.

The source exhibits complex variability over the orbital period, featuring both absorption dips and flaring in the X-ray band. The effects of this on the ASM light curve can easily be seen in Figure 1 (upper panel). Figure 1 (lower panel) shows a zoomed-in ASM light curve of two full orbital cycles extracted from $\text{JD} = 50363.4$ to $\text{JD} = 50396.6$, which corresponds to the time duration marked in the upper panel. We define the region $-0.1 < \phi < 0.2$ as the flaring stage and the region $0.2 < \phi < 0.9$ as the non-flaring stage (Shirey et al. 1996).

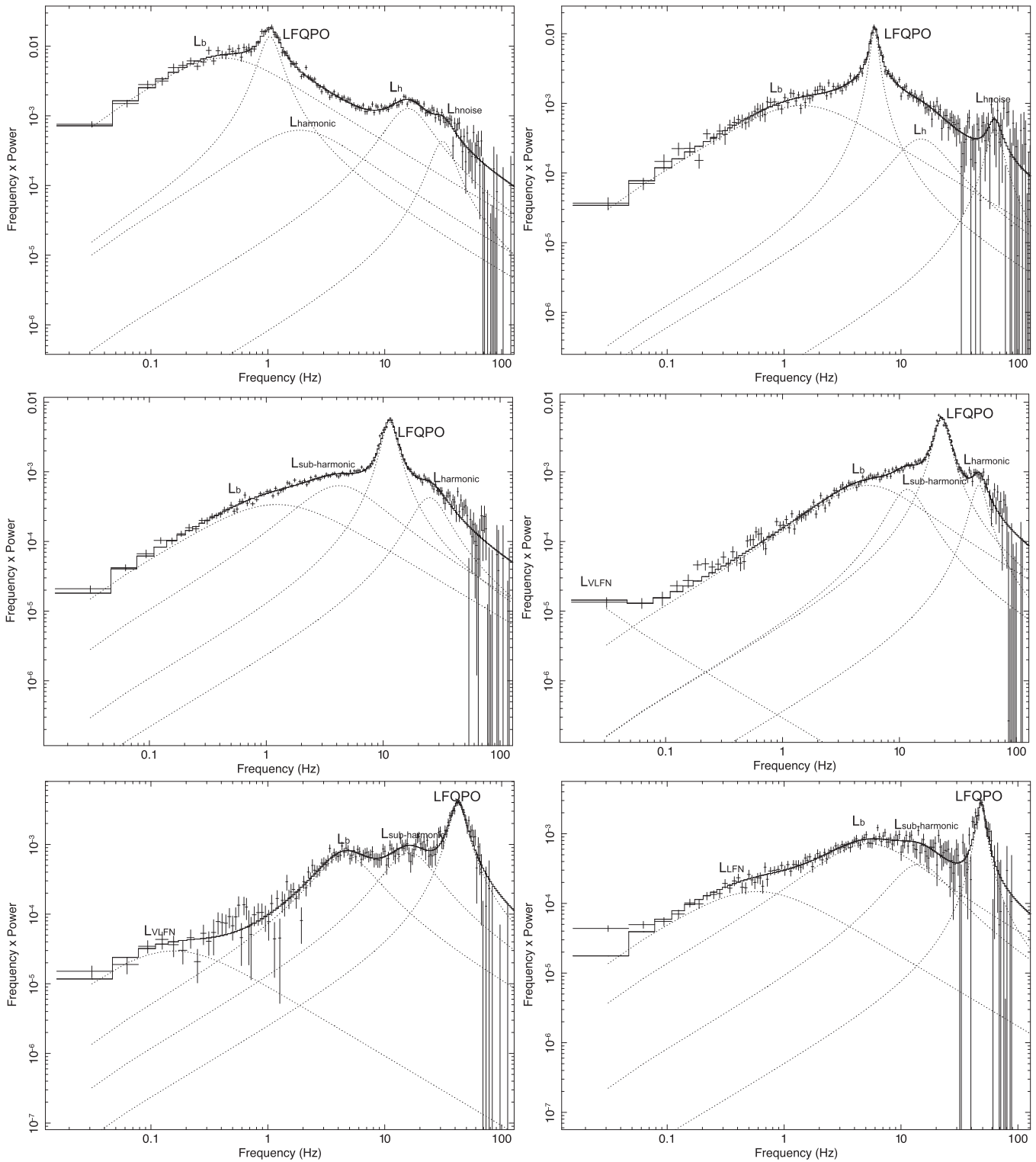


Figure 5. Six representative PDSs of Cir X-1 together with their best-fit components. L_{VLFN} , L_{LFN} , L_b , L_{subh} , LFQPO, $L_{harmonic}$, L_h , and L_{hnoise} are labeled in the figure. The following *RXTE* ObsIDs were used: from left to right, top to bottom, 30081-06-03-03, 20097-01-24-00, 20095-01-11-00, 20095-01-23-01, 70020-01-02-02, and 80027-01-05-01.

To better understand how the LFQPO properties evolve as a function of phase, we plot the LFQPO centroid frequency as a function of orbital phase in Figure 10. Each dot represents an observation with QPO, and the dashed lines separate the flaring stage from the non-flaring stage. LFQPOs detected in the atoll state are plotted separately as blue dots; confirmed HBOs are

marked as red dots. The points reported by Shirey et al. (1996) are marked as black stars. The LFQPO frequency shows additional scattering in the 0.2–0.5 range, while in the 0.5–0.9 range it is comparable to the flaring stage. Comparing the numbers of QPO detections with the number of observations, we find that the frequency of QPO detections is higher in the

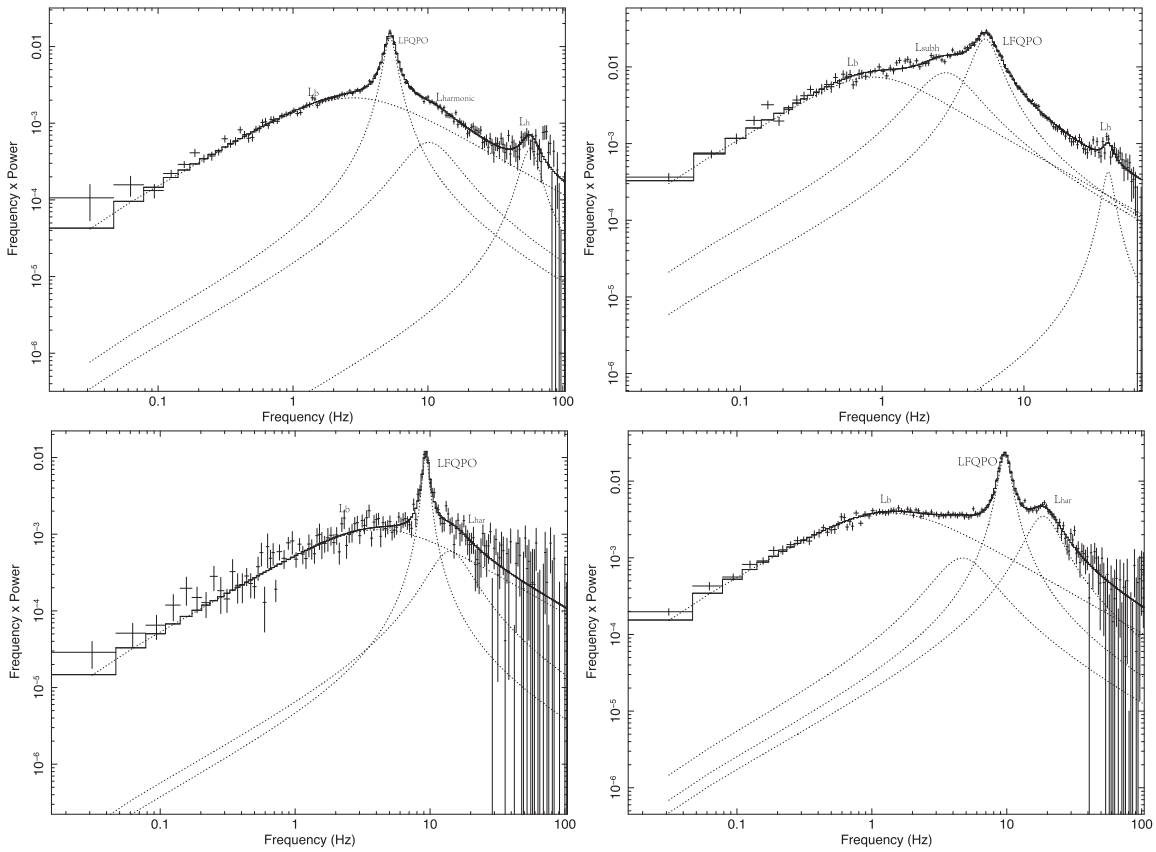


Figure 6. Comparison of power spectra of Cir X-1 QPO without (left panels) or with (right panels) sub-harmonics for the same QPO frequency (~ 5 Hz for the top panels, ~ 10 Hz for the bottom panels). Observations are 10122-01-11-01, 20071-01-07-00, 30080-01-01-12, and 70020-01-04-01 from left to right, top to bottom.

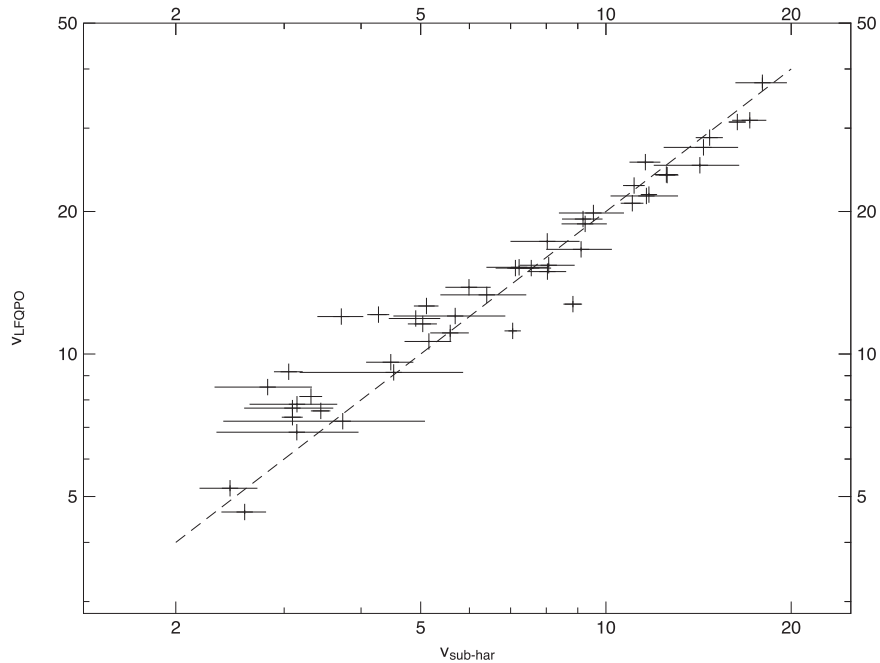


Figure 7. Centroid frequency of the component L_{LF} as a function of centroid frequency of its associated L_{subh} component. The dashed line represents $y = 2 * x$.

non-flaring stage ($20\% \pm 2\%$) than in the flaring stage ($11\% \pm 2\%$). We plot the rms phase dependence for all of the observations in Figure 11. Again, blue and red dots represent LFQPOs from the atoll state and HBOs; red stars are

points from Shirey et al. (1996). Dotted lines separate the non-flaring phase from the flaring phase. The fractional rms shows a large scatter during orbital phase 0–0.5 and decreases slightly after phase 0.5.

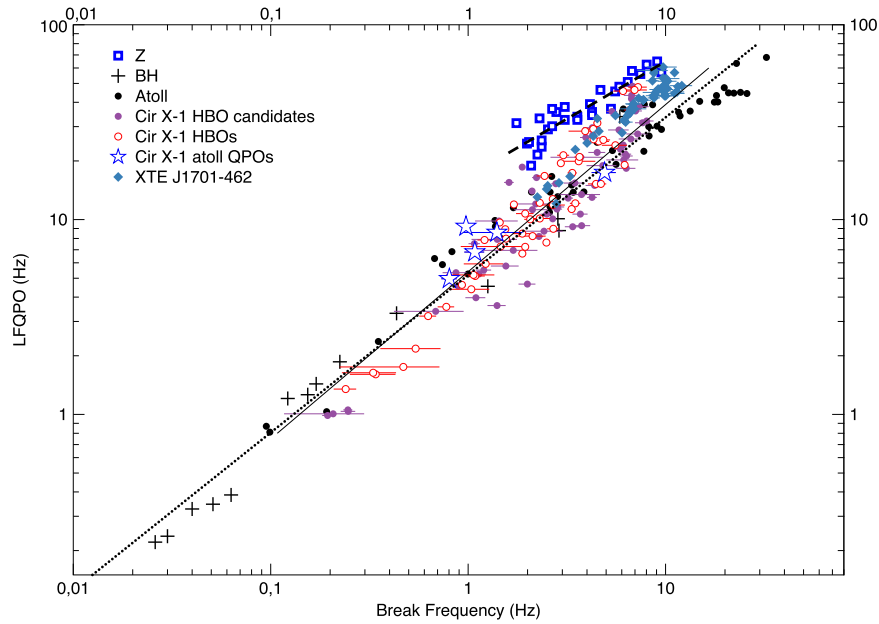


Figure 8. LFQPO frequency as a function of break frequency (the WK correlation), including HBOs from Cir X-1 (red circles), HBO candidates (purple filled circles), and LFQPOs (blue stars) from the atoll state of Cir X-1. Black hole (black crosses) and atoll (filled black circles) sources from Wijnands & van der Klis (1999), Z sources (open blue squares) from Wijnands & van der Klis (1999), and XTE J1701-462 (filled cyan squares) from Bu et al. (2015). The lines are power-law fits to BH/atoll (dotted line), Z sources (dashed line), and Cir X-1 (filled line).

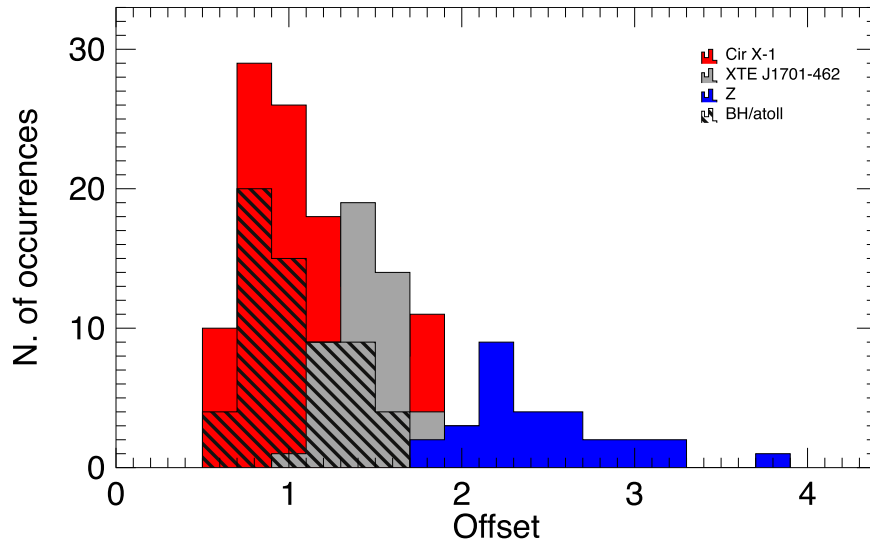


Figure 9. Histogram distribution of the offset from the fitting line of BH/atoll ($\nu_{\text{LFQPO}} = (5.2 \pm 0.32) * \nu_{\text{break}}^{(0.81 \pm 0.03)}$). Offset indicates how far a point would shift from the fitting line at a certain break frequency, with the colors indicating different sources.

4. Discussion

4.1. The WK Correlation in Cir X-1 and Z Sources

The PDS of Cir X-1 are very similar to those found in typical Z sources, and the correlation between kHz QPOs and LFQPOs (PBK correlation) is in good agreement with that found previously in Z sources (Boutloukos et al. 2006), suggesting that Cir X-1 is a Z source. Cir X-1 has the widest HBO frequency range among Z sources, from ~ 1 to ~ 50 Hz, which allows us to extend the correlation for Z sources, which previously consisted of a narrow group of points above the BH/atoll correlation (Wijnands & van der Klis 1999). Besides, it is also the first time that LFQPOs have been reported in the atoll state of Cir X-1, which allows us to make a direct comparison between HBOs and LFQPOs from the atoll state

within the same system. As can be seen from Figures 4 and 8, LFQPOs from the atoll state show great consistency with HBOs in both timing features and WK correlation, which suggests that LFQPOs in the atoll state probably evolved from the HBOs in the Z state. Some of the detections might be from an unrecognized atoll state, but this would not change our conclusions.

In Figure 8 (WK correlation), the Cir X-1 points follow the general BH/atoll correlation and overlap with XTE 1701-462 as well. Hence, Z sources show two different tracks in the WK scheme, XTE J1701-462 and Cir X-1 are following the BH/atoll correlation, while the persistent Z sources shifted upward from the main correlation (see the blue squares in Figure 7, which include all the Z systems that have been reported). Persistent Z sources generally have higher luminosities than

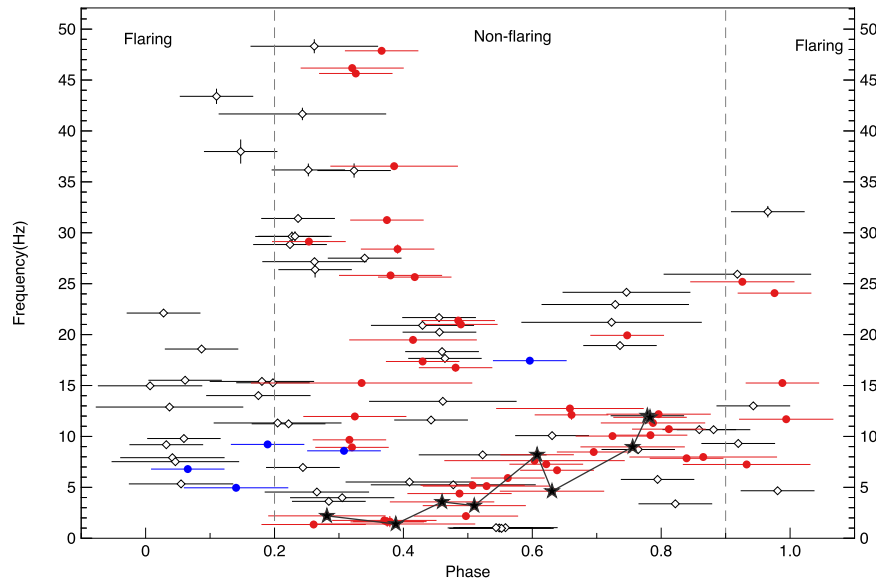


Figure 10. LFQPO frequency as a function of orbital phase. The dashed lines separate the flaring stage ($0.9 < \phi < 0.2$) from the non-flaring phase ($0.2 < \phi < 0.9$). Points from Shirey et al. (1996) are marked as black stars. Open diamonds, red dots, and blue dots represent HBO candidates, HBOs, and LFQPOs from the atoll state of Cir X-1, respectively.

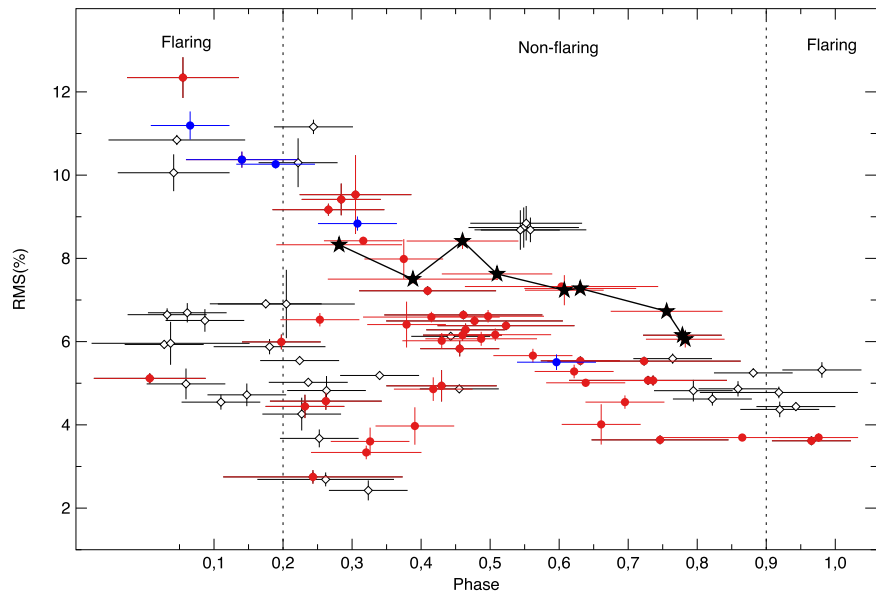


Figure 11. LFQPO fractional rms as a function of orbital phase. The dashed lines separate the flaring stage ($0.9 < \phi < 0.2$) from the non-flaring phase ($0.2 < \phi < 0.9$). Points from Shirey et al. (1996) are marked as black stars. Open diamonds, red dots, and blue dots represent HBO candidates, HBOs, and LFQPOs from the atoll state of Cir X-1, respectively.

atoll and BH sources. In order to check whether the shift is caused by luminosity, we investigated the total luminosity of HBs for all the Z sources. GX 17+2 has the highest luminosity of all five persistent Z systems, $1.44\text{--}1.55 L_{\text{Edd}}$ (Lin et al. 2012), while GX 340+0 has the lowest luminosity $0.3\text{--}0.7 L_{\text{Edd}}$ (Seifina et al. 2013). For the transitional Z systems XTE J1701-462 and Cir X-1, it is interesting to find that they have a similar luminosity range as persistent Z systems, $0.44\text{--}0.91 L_{\text{Edd}}$ for the former (Li et al. 2013) and $1.2\text{--}1.8 L_{\text{Edd}}$ for the latter (Ding et al. 2012). This means that neither luminosity nor mass accretion rate are related to the shift of persistent Z systems.

In Figure 8, for given break frequencies, the frequencies of HBOs from persistent Z systems are 2–2.5 times higher than those

from other systems. One possibility is that HBOs observed in persistent Z sources are the second harmonics instead of fundamentals, as already suggested by Wijnands & van der Klis (1999). From the PDS fitting results from Cir X-1 and XTE J1701-462, we see that HBOs with higher frequencies tend to have stronger sub-harmonics components. This supports the hypothesis that in persistent Z systems the fundamentals were misidentified as sub-harmonics. Wijnands & van der Klis (1999) excluded this possibility because of the PBK correlation, where Z sources follow the same correlation as BH and atoll sources. However, we note that some points from atoll systems (i.e., 4U 1608-42, 4U 1728-34) also shifted downward from the PBK correlation by a factor of about 2 (Psaltis et al. 1999). Therefore, it is also possible that in the PBK at times the LFQPO is misidentified.

Besides LFQPO frequencies, the WK correlation can also be offset by changes in the break frequency. As mentioned above, the value of ν_b is affected by its nearby LFQPO or sub-harmonic component. However, the sub-harmonic is not always detected significantly. Boutloukos et al. (2006) also studied the timing features of Cir X-1 and found scattering of L_b for certain values of LFQPOs. They suggested that the scattering is caused by two sets of break frequency components. However, after we added a sub-harmonic component in our fit models, the scattering of L_b had obviously reduced. In this case, the second break component mentioned in Boutloukos et al. (2006) could be a non-significant sub-harmonic component.

Our results show that the two transitional Z sources XTE J1701-462 and Cir X-1 lie close to the atoll/BH branch of the WK correlation, offset from the branch of persistent Z sources. We have shown that the presence of a second branch is compatible with being due to a misidentification of the fundamental frequency of the HBO. This dichotomy appears to be visible also in the high-frequency part of the PBK correlation (Psaltis et al. 1999; Belloni et al. 2002).

A model for HBOs based on relativistic LT precession has been proposed by Stella & Vietri (1998). Within this model, the kHz QPOs found in NS binaries are also associated to relativistic frequencies, and it explains naturally the PBK correlation (Stella et al. 1999). This model, which only considers fundamental frequencies set by General Relativity at a single radius, does not address the flat-top noise component and therefore the WK correlation. This model applies both to BH and NS sources. Ingram et al. (2009) and Ingram & Done (2010) proposed a more complex model based on the same frequencies involving the LT precession of a hot inner flow within a truncated accretion disk. Within this model, the flat-top noise arises from variations in mass accretion rate from the outer regions of the accretion flow that propagate inward.

Interestingly, Stella & Vietri (1998) noticed that their model in the case of NS sources would interpret the data in a more complete way if the observed HBO frequency was twice that given by LT precession, which is precisely what we find here. Moreover, we show that this misidentification of the physical frequency by a factor of 2 is not related to the Z-atoll classification, as Z sources also populate the lower branch in the WK correlation.

4.2. The Orbital Phase Influence on the LFQPO in Cir X-1

For Cir X-1, because of its high eccentricity, the mass accretion rate is a strong function of the orbital position of the compact star relative to the primary star. Most of the mass transfer occurs near the periastron, after which mass transfer from the companion to the accretion disk ceases (Ding et al. 2012), therefore making X-ray emission of this sources strongly phase dependent. In Figures 10 and 11, we show plots of QPO frequency and fractional rms as functions of orbital phase. Points from the atoll state, Z states, and Shirey et al. (1996) are also included in these plots. As can be seen from the plots, there is a large scatter and no clear evidence suggesting that QPO properties are affected by orbital phase. Shirey et al. (1996) reported that QPO features evolve with orbital phase. However, as can be seen from Figure 1, the points from Shirey et al. (1996) only covered a small range of the earliest *RXTE* observations. When a large number of observations is considered, LFQPOs properties appear not to be related to orbital phase.

5. Summary

We thank the anonymous referee for helpful comments and valuable suggestions. This research has made use of data obtained from the High Energy Astrophysics Science Achieve Research Center (HEASARC) provided by NASA Goddard Space Flight Center. This work is supported partially by the Chinese Scholarship Council, National Natural Science Foundation of China, NSFC 11173024, 11543008, 11673023, and the National Key Research and Development Program of China (2016YFA0400800).

References

- Altamirano, D., Ingram, A., van der Klis, M., et al. 2012, *ApJL*, **759**, L20
 Arnaud, K. A. 1996, in ASP Conf. Ser. 101, *Astronomical Data Analysis Software and Systems V*, ed. G. H. Jacoby & J. Barnes (San Francisco, CA: ASP), 17
 Belloni, T., & Hasinger, G. 1990, *A&A*, **230**, 103
 Belloni, T., Homan, J., Motta, S., Ratti, E., & Méndez, M. 2007, *MNRAS*, **379**, 247
 Belloni, T., Psaltis, D., & van der Kils, M. 2002, *ApJ*, **572**, 392
 Boutloukos, S., Van Der Klis, M., Altamirano, D., et al. 2006, *ApJ*, **653**, 1435
 Bu, Q., Chen, L., Li, Z., Qu, J., & Belloni, T. 2015, *ApJ*, **799**, 2
 Casella, P., Belloni, T., Homan, J., & Stella, L. 2004, *A&A*, **426**, 587
 Casella, P., Belloni, T., & Stella, L. 2005, *ApJ*, **629**, 403
 Cui, W., Zhang, S. N., & Chen, W. 2000, *ApJL*, **526**, L33
 Ding, G., Huang, C., & Qu, J. 2012, *IJAA*, **2**, 256
 Ding, G. Q., Zhang, S. N., Li, T. P., & Qu, J. L. 2006, *ApJ*, **645**, 576
 Fridriksson, J. K., Homan, J., & Remillard, R. A. 2015, *ApJ*, **809**, 52
 Hasinger, G., & van der Klis, M. 1989, *A&A*, **225**, 79
 Homan, J. 2012, *ApJL*, **760**, L30
 Homan, J., Fridriksson, J. K., & Remillard, R. A. 2015, *ApJ*, **812**, 80
 Homan, J., van der Klis, M., Jonker, P. G., et al. 2002, *ApJ*, **568**, 878
 Ingram, A., & Done, C. 2010, *MNRAS*, **405**, 2447
 Ingram, A., Done, C., & Fragile, P. C. 2009, *MNRAS*, **397**, L101
 Kaluzienski, L. J., Holt, S. S., Boldt, E. A., & Serlemitsos, P. J. 1976, *ApJ*, **208**, L71
 Li, Z. S., Chen, L., Qu, J. L., et al. 2013, *ApJ*, **767**, 167
 Li, Z. S., Chen, L., Qu, J. L., et al. 2014, *ApJ*, **786**, 119
 Lin, D., Remillard, R. A., Homan, J., & Barret, D. 2012, *ApJ*, **756**, 34
 Linares, M., Soleri, P., Watts, A., Altamirano, D., et al. 2010, *ATel*, **2643**, 1
 Motta, S., Belloni, T. M., Stella, L., Muñoz-Darias, T., & Fender, R. 2015a, *MNRAS*, **437**, 2554
 Motta, S., Casella, P., Henze, M., et al. 2015b, *MNRAS*, **447**, 2059
 Motta, S. E. 2016, *AN*, **337**, 398
 Motta, S. E., Muñoz-Darias, T., Casella, P., Belloni, T. M., & Homan, J. 2011, *MNRAS*, **418**, 2292
 Nowak, M. A. 2000, *MNRAS*, **318**, 361
 Oosterbroek, T., Van der Klis, M., Kuulkers, E., et al. 1995, *A&A*, **297**, 141
 Parkinson, P. M., Tournear, D. M., Bloom, E. D., et al. 2003, *ApJ*, **595**, 333
 Psaltis, D., Belloni, T., & van der Klis, M. 1999, *ApJ*, **520**, 262
 Qu, J. L., Yu, W. F., & Li, T. P. 2001, *ApJ*, **555**, 7
 Remillard, R. A., Sobczak, G. J., Munro, M. P., & McClintock, J. E. 2002, *ApJ*, **564**, 962
 Schnittman, J. D., Homan, J., & Miller, J. M. 2006, *ApJ*, **642**, 420
 Seifina, E., Titarchuk, L., & Frontera, F. 2013, *ApJ*, **766**, 63
 Shirey, R. E. 1998, PhD thesis, MIT
 Shirey, R. E., Bradt, H. V., Levine, A. M., & Morgan, E. H. 1996, *ApJL*, **469**, L21
 Shirey, R. E., Bradt, H. V., Levine, A. M., & Morgan, E. H. 1998, *ApJ*, **506**, 374
 Stella, L., & Vietri, M. 1998, *ApJL*, **492**, L59
 Stella, L., Vietri, M., & Morsink, S. M. 1999, *ApJ*, **524**, 63
 Tagger, M., & Pellat, R. 1999, *A&A*, **349**, 1003
 Titarchuk, L., & Osherovich, V. 1999, *ApJL*, **518**, L95
 van der Klis, M. 2006, in *Compact Stellar X-ray Sources*, ed. W. H. G. Lewin & M. van der Klis (Cambridge: Cambridge Univ. Press), 56
 Wijnands, R., Homan, J., & van der Klis, M. 1999, *ApJL*, **526**, L33
 Wijnands, R., & van der Klis, M. 1999, *ApJ*, **514**, 939
 Zhang, S. N. 2013, *FrPhy*, **8**, 630